oceans

Article

Global Chlorophyll Concentration Distribution and Effects on Bottom Reflectance of Coral Reefs

Ana G. Bonelli *, Paulina Martin, Phillip Noel and Gregory P. Asner

Center for Global Discovery and Conservation Science, Arizona State University, Tempe, AZ 85287, USA; paulinam@asu.edu (P.M.); phillno@asu.edu (P.N.); gregasner@asu.edu (G.P.A.)

* Correspondence: abonelli@asu.edu

Abstract: Despite the limited coverage of coral reefs in the world's oceans, they play a crucial role in global marine biodiversity and providing essential ecosystem services. This study explores the influence of chlorophyll-a (*Chl-a*) concentration in the water column on the estimation of bottom reflectance (r_b) in coral reefs monitored by the Allen Coral Atlas coral reef monitoring system, using satellite imagery from a Sentinel-2 MSI sensor. We conducted a comprehensive analysis, considering *Chl-a* global distribution and variability, and its combined effect with water column depth over r_b calculation. Our results demonstrated that the impact of *Chl-a* on r_b estimation becomes significant when the water column depth exceeds 3 m. While suggesting the optionality of using regional *Chl-a* values, our study highlights potential overestimations of *Chl-a* in optically complex environments, such as along the Brazilian coast. This research contributes to refining coral reef monitoring systems and underscores the importance of accurate *Chl-a* assessments for robust environmental evaluations.

Keywords: chlorophyll-a; bottom reflectance; water column correction; coral reefs; ocean color; remote sensing

Citation: Bonelli, A.G.; Martin, P.; Noel, P.; Asner, G.P. Global Chlorophyll Concentration Distribution and Effects on Bottom Reflectance of Coral Reefs. *Oceans* **2024**, *5*, 210–226. https://doi.org/10.3390/oceans5020013

Academic Editors: Giacomo De Carolis, Gianfranco Fornaro, Sedat Gündoğdu, Giovanni Ludeno, Matteo Postacchini, Ali Rıza Kosker and Virginia Zamparelli

Received: 19 January 2024
Revised: 19 March 2024
Accepted: 29 March 2024
Published: 10 April 2024

1. Introduction

Shallow coral reefs cover a small portion of global oceans but support upwards of 25% of global marine biodiversity [1–4]. Reefs also support coastal protection, food, and recreation for neighboring human populations as well as being a global-scale food and recreational source [5–7]. Despite their significance, coral reef ecosystems face increasing threats such as extensive exploitation, resulting in their global deterioration [8].

Mapping and monitoring coral reefs plays a major role in developing and implementing effective management strategies [9]. Reef bottom reflectance (r_b) provides information needed to monitor changes in benthic composition and state [10]. Multispectral remote sensing continues to be a growing tool for assessing changes in bottom reflectance, but to account for the interference of water in pursuit of the seafloor signal, it is necessary to separate the components of the bottom reflectance from water column scattering and absorption processes.

The Allen Coral Atlas coral reef monitoring system utilizes Sentinel-2 L2A/B satellite imagery to detect changes in benthic color reflectance and to assign detected changes in benthic reflectance to potential coral bleaching. Estimating benthic reflectance requires an effort to minimize the water column signal by estimating the optical properties of the water column. Several algorithms have been implemented to obtain these water column properties, such as absorption and backscattering coefficients, which are highly dependent on the concentration of chlorophyll-a (*Chl-a*) in seawater (Figure 1). Despite a known dependence of the Allen Coral Atlas coral reef monitoring system on water column *Chl-a*, the beta version of the Atlas system employed a fixed global *Chl-a* value of 0.5 mg·m^{-3}.

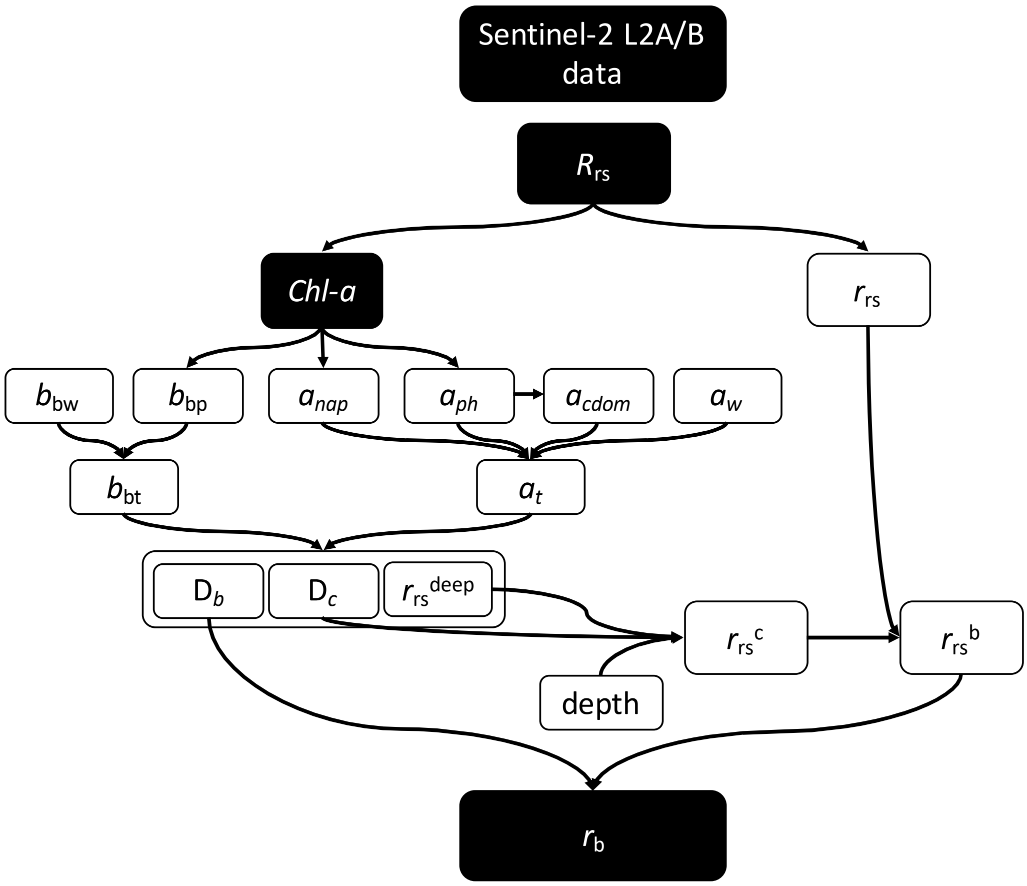

Figure 1. Methodology flowchart used by the Allen Coral Atlas' to calculate the r_b from Sentinel-2 satellite data. For symbol definitions see Table 1.

Table 1. Definition of terms, units, and abbreviations.

	Units	Definition
$a_{cdom}(\lambda)$	m^{-1}	Absorption coefficient of chromophoric dissolved organic mater
$a_{nap}(\lambda)$	m^{-1}	Absorption coefficient of non-algal particles
$a_{ph}(\lambda)$	m^{-1}	Absorption coefficient of phytoplankton pigments
$a_t(\lambda)$	m^{-1}	Absorption coefficient of the total ($a_w + a_{cdom} + a_{ph} + a_{nap}$)
$a_w(\lambda)$	m^{-1}	Absorption coefficient of pure seawater
$b_{bp}(\lambda)$	m^{-1}	Backscattering coefficient of suspended particles
$b_{bt}(\lambda)$	m^{-1}	Backscattering coefficient of the total, $b_{bw} + b_{bp}$
$b_{bw}(\lambda)$	m^{-1}	Backscattering coefficient of pure seawater
Chl-a	$mg{\cdot}m^{-3}$	Chlorophyll-a concentration
D_b		Distribution function that relates the vertically averaged diffuse attenuation coefficient for upwelling radiance from bottom reflectance to a_t and b_t
D_c		Distribution function that relates the vertically averaged diffuse attenuation coefficient for upwelling radiance from water-column scattering to a_t and b_t
r_{rs}	sr^{-1}	Below-surface remote sensing reflectance
$r_{rs}{}^{b}$	sr^{-1}	Below-surface remote sensing reflectance from bottom reflection
$r_{rs}{}^{c}$	sr^{-1}	Below-surface remote sensing reflectance from water column scattering
$r_{rs}{}^{deep}$		Below-surface remote sensing reflectance when the water depth is infinite
r_b		Bottom reflectance
R_{rs}	sr^{-1}	Above-surface remote sensing reflectance

Here, we aimed to determine the effects of *Chl-a* on r_b estimation. To achieve this, we addressed two key questions: (1) What is the global distribution and variability of water column *Chl-a* over coral reefs? (2) How does the variability of *Chl-a* affect the estimation of r_b on coral reefs? In answering these questions, we sought to improve the Allen Coral Atlas coral reef detection system while also providing general insight on *Chl-a* estimation that might assist in other oceanographic programs. Our findings contribute to improving our understanding of the current state and the changes underway in coral reef ecosystems worldwide.

2. Materials and Methods

In this study, we target coral reefs gathered within the 214 globally distributed regions of the NOAA-CRW Regional Virtual Stations (https://coralreefwatch.noaa.gov/product/vs/data.php (accessed on 24 March 2023)). These regions encompass numerous geographic locations, capturing the diversity and associated challenges present in coral reef environments worldwide.

Our analysis specifically centers on coral reefs classified as the benthic "coral/algae" category in the Allen Coral Atlas. It is important to note that this category only includes coral reefs to a maximum depth of 10 m, as this is the maximum depth that can be accurately monitored with multispectral satellite imagery [11].

2.1. Satellite Data

We utilized a time series of Sentinel-2 L2A/B satellite data spanning from 1 January 2019 to 31 December 2022. Sentinel-2 MSI provides data with a spatial resolution of 10 m, 20 m, and 60 m. The data were acquired and processed through Google Earth Engine (GEE). GEE retrieves the data from Sentinel Hub and performs the atmospheric correction implementing sen2cor (https://step.esa.int/main/snap-supported-plugins/sen2cor/ (accessed on 24 March 2023)), which also generates a Scene Classification Map (SCL) band with a 20 m resolution. Utilizing information from the SCL and the QA60 (Quality Assessment 60-m resolution) bands provided with the Sentinel-2 imagery, we identified clouds and cloud shadows and masked them out. The QA60 band offers indicators related to cloud probability and atmospheric conditions (https://sentinel.esa.int/web/sentinel/technical-guides/sentinel-2-msi/level-1c/cloud-masks (accessed 24 March 2023)). Additionally, the SCL band categorizes pixels into various land cover classes, including water bodies and clouds, thereby aiding in cloud detection (https://custom-scripts.sentinel-hub.com/custom-scripts/sentinel-2/scene-classification/ (accessed on 24 March 2023)). Leveraging this information, we implemented the maskS2clouds() function from Google Earth Engine (GEE) (https://developers.google.com/earth-engine/datasets/catalog/COPERNICUS_S2_SR (accessed on 24 March 2023)) to generate clean, cloud-free imagery. The maskS2clouds() function internally resamples the cloud and shadow masks derived from the QA60 and SCL bands to match the resolution of the target bands, ensuring accurate application of the masks to all bands.

2.2. Chl-a Calculation

Chl-a is a central component in the computation of r_b. The areas monitored by the atlas are located in the tropical oceans. Generally, tropical reefs occur in highly oligotrophic oceanic water, systems where the water column nutrients are characteristically low [12]. Therefore, to compute the satellite-derived *Chl-a* from the above-surface remote sensing reflectance (R_{rs}) we tested the implementation of the approach described by [13]:

$$\text{Chl-}a = 10^{(-0.4909+191.659\times\omega)} \quad (1)$$

where ω is the weighted relative difference between $R_{rs}(443)$ and $R_{rs}(555)$, computed as follows:

$$\omega = R_{rs}(560) - 0.46 \times R_{rs}(443) - 0.54 \times R_{rs}(670) \quad (2)$$

In [13], the authors demonstrated the strong correlation between satellite-derived *Chl-a* and in situ *Chl-a* over a wide range of concentrations (0.03–10 mg·m^{-3}) when applied to MODIS-Aqua satellite data. It has been demonstrated that MODIS-Aqua reflectance is in good agreement with Sentinel-2 L2A/2B MSI reflectance [14]. Thus, we believe this algorithm (Equations (1) and (2)) can be implemented to estimate *Chl-a* for the Allen Coral Atlas coral reef monitoring system, based on Sentinel-2 L2A/2B MSI data.

The computation of *Chl-a* was exclusively conducted for pixels within the regional polygons that contain coral reefs. Initially, an image collection was assembled for each region, consolidating data from 1 January 2019 to 31 December 2022, masking clouds and shadows (see Section 2.1). Subsequently, a mask assembling the areas corresponding to the coral/algae class from the benthic maps available on the ACA website (https://allencoralatlas.org/atlas/#1.00/0.0000/-145.0000 (accessed on 24 March 2023)) was generated for each region. Only pixels falling within the coral/algae category were used for subsequent computation.

Bands 2 (490 nm), 3 (560 nm), and 4 (665 nm) were selected and independently averaged, followed by the calculation of *Chl-a* for each of the remaining pixels. To mitigate the influence of outliers, pixels exhibiting *Chl-a* values surpassing 100 mg·m^{-3} were systematically excluded, as they deviate from the anticipated *Chl-a* in the ocean [15]. Moreover, the global mean and standard deviation of *Chl-a* were computed, establishing a threshold as the global mean plus one standard deviation. Pixels exceeding this threshold were masked.

Finally, for each region, the mean *Chl-a* (m*Chl-a*) was computed by spatially averaging the pixel values.

2.3. Bottom Reflectance Calculation

r_b was calculated from above-surface remote sensing reflectance (R_{rs}) following the methodology proposed by [16]. Their model requires assessing the below-surface remote sensing reflectance (r_{rs}) and isolating the signal of its contributors: the water column scattering (${r_{rs}}^c$) and the bottom reflectance (${r_{rs}}^b$). r_{rs} were derived from $R_{rs}(\lambda)$ as defined by [17].

$$r_{rs}(\lambda) = \frac{R_{rs}(\lambda)}{0.52 + 1.7R_{rs}(\lambda)} \tag{3}$$

Furthermore, r_{rs} can also be expressed as the summation of the water column constituent and the bottom constituent (Equation (4)).

$$r_{rs}(\lambda) = {r_{rs}}^b(\lambda) + {r_{rs}}^c(\lambda) \tag{4}$$

$${r_{rs}}^c(\lambda) = r_{rs}^{deep}\left(1 - e^{-D_c(a_t+b_b)\mathrm{H}}\right) \tag{5}$$

$${r_{rs}}^b(\lambda) = \frac{1}{\pi} r_b(\lambda) e^{-D_b(a_t+b_b)\mathrm{H}} \tag{6}$$

In Equations (5) and (6), a_t indicates the total absorption of the water column, b_b represents the total backscattering of the water column, and H denotes the depth of the water column under consideration. For our calculations, we used the satellite-derived depth from the Allen Coral Atlas calculated implementing the methodology described by [18].

Furthermore, D_c stands as an empirical parameter accounting for the under-water photon path elongation due to scattering effects within the water columns ([19]; Equation (7)) and D_b is the light attenuation of the bottom reflectance ([19]; Equation (8)). Lastly, r_{rs}^{deep} represents r_{rs} in infinitely deep water, and it was derived from the total absorption (a_t) and total backscattering (b_b) of the water column (Equation (9)).

$$D_c = 1.03(1 + 2.4\frac{b_b}{a_t + b_b})^{0.5} \tag{7}$$

$$D_{\mathrm{b}} = 1.05(1 + 5.5\frac{b_{\mathrm{b}}}{a_{\mathrm{t}} + b_{\mathrm{b}}})^{0.5} \tag{8}$$

$$r_{\mathrm{rs}}^{\mathrm{deep}} = \left(0.089 + 0.125\frac{b_{\mathrm{b}}}{a_{\mathrm{t}} + b_{\mathrm{b}}}\right)\frac{b_{\mathrm{b}}}{a_{\mathrm{t}} + b_{\mathrm{b}}} \tag{9}$$

Hence, by rearranging Equation (6), r_b was formulated as follows:

$$r_{\mathrm{b}}(\lambda) = \frac{{r_{\mathrm{rs}}}^{\mathrm{b}}(\lambda) * \pi}{e^{-D_{\mathrm{b}}(a_{\mathrm{t}}+b_{\mathrm{b}})H}} \tag{10}$$

a_{t} entails the summation of the absorption from three distinct constituents: the absorption coefficient of pure water (a_{w}), the absorption of phytoplankton ($a_{\mathrm{ph}}(\lambda)$), and the absorption of colored dissolved organic matter ($a_{\mathrm{cdom}}(\lambda)$) (Equation (11)).

$$a_{\mathrm{t}}(\lambda) = a_{\mathrm{w}}(\lambda) + \mathrm{a}_{\mathrm{ph}}(\lambda) + a_{\mathrm{nap}}(\lambda) + a_{\mathrm{cdom}}(\lambda) \tag{11}$$

While a_{w} is a known value [20], $a_{\mathrm{ph}}(\lambda)$, $a_{\mathrm{nap}}(\lambda)$, and $a_{\mathrm{cdom}}(\lambda)$ are derived from satellite data. As described by [21], $a_{\mathrm{ph}}(\lambda)$ is determined based on satellite-derived *Chl-a*

$$a_{\mathrm{ph}}(\lambda) = \left[a_0(\lambda) + a_1(\lambda) \times ln\left(a_{\mathrm{ph}}(440)\right)\right] \times a_{\mathrm{ph}}(440) \tag{12}$$

$$a_{\mathrm{ph}}(440) = 0.06 \times [Chl - a]^{0.65} \tag{13}$$

where $a_0(\lambda)$ and $a_1(\lambda)$ are known values from [22] QAA(v5).

Afterwards, $a_{\mathrm{nap}}(\lambda)$ was derived from $a_{\mathrm{ph}}(440)$ implementing the model formulated by [23,24].

$$a_{\mathrm{nap}}(\lambda) = a_{\mathrm{nap}}(440) \times e^{-S_{\mathrm{nap}}(\lambda-440)} \tag{14}$$

$$a_{\mathrm{nap}}(440) = 0.0124 \times [Chl - a]^{0.724} \tag{15}$$

where $e^{-S(\lambda-440)}$ with S_{nap} = 0.011 is the globally average slope of the exponential function representing the spectral dependence of a_{nap}.

Similarly, $a_{\mathrm{cdom}}(\lambda)$ was derived from $a_{\mathrm{ph}}(440)$ implementing the model formulated by [23,24].

$$a_{\mathrm{cdom}}(\lambda) = a_{\mathrm{cdom}}(440) \times e^{-S(\lambda-440)} \tag{16}$$

$$a_{\mathrm{cdom}}(440) = 0.5 \times a_{\mathrm{ph}}(440) \tag{17}$$

where $e^{-S(\lambda-440)}$ with S = 0.015 is the globally average slope of locally produced chromophoric dissolved organic matter.

Furthermore, b_{bt} was calculated as the summation of the backscattering of pure water (b_{bw}) and the backscattering of particles (b_{bp}).

$$b_{\mathrm{bt}}(\lambda) = b_{\mathrm{bw}}(\lambda) + b_{\mathrm{bp}}(\lambda) \tag{18}$$

where b_{bw} is a known value [25] and b_{bp} was estimated from satellite-derived *Chl-a* as described by [24].

$$b_{\mathrm{bp}}(\lambda) = \left\{0.002 + 0.02[0.5 - 0.25 \times log_{10}(Chl\text{-}a)] \times \left(\frac{550}{\lambda}\right)\right\} \times b_{\mathrm{bp}}(555) \tag{19}$$

$$b_{\mathrm{bp}}(555) = 0.6 \times (Chl\text{-}a)^{0.62} \tag{20}$$

2.4. Satellite-Derived mChl-a Validation

m*Chl-a* validation was conducted by comparing satellite-derived values with an in situ regional mean Chlorophyll-a concentration (m*Chl-a*$_{is}$) dataset. The m*Chl-a*$_{is}$ dataset was built by gathering *Chl-a* data from the NASA SeaBASS [26] database spanning from the years 2000 to 2022. Notably, the in situ dataset covered a wider time range than that utilized for calculating m*Chl-a*, as there were no matching data available between 2019 and 2022. Additionally, only *Chl-a* measurements taken up to a depth of 10 m were considered in the analysis, aligning with the maximum depth covered by the Allen Coral Atlas coral bleaching monitoring system. After thoroughly filtering the dataset and averaging the regional in situ *Chl-a* concentration data, nine matching regions were identified. (Figure 2). Subsequently m$Chl\text{-}a_{is}$ was compared to the satellite-derived m*Chl-a* values to assess the accuracy of our estimation (see Section 3).

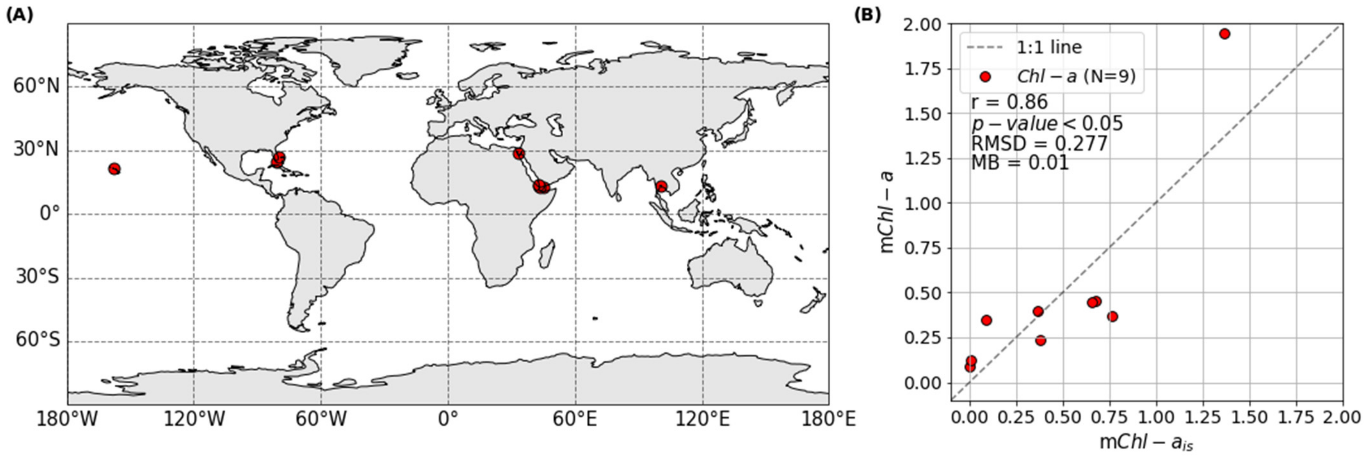

Figure 2. (**A**) Map of the locations where $Chl\text{-}a_{is}$ matched satellite-derived m*Chl-a*. (**B**) Scatter plot and statistics of m*Chl-a* vs. $Chl\text{-}a_{is}$.

This evaluation involved visually comparing m*Chl-a* versus m$Chl\text{-}a_{is}$, supported by the Pearson correlation coefficient (r), the root mean square deviation (RMSD, Equation (21)), and the mean bias (MB, Equation (22)).

$$\mathrm{RMSD} = \sqrt{\sum_{i=1}^{N} \frac{(yi - xi)^2}{n}} \tag{21}$$

$$\mathrm{MB} = \sqrt{\frac{mean(yi)}{mean(xi)}} \tag{22}$$

where *yi* and *xi* are the estimated and in situ values, respectively.

2.5. Satellite-Derived Chl-a Spatial Distribution Variability

A global map of satellite-derived m*Chl-a* was generated, and its distribution and variability were assessed through a combination of graphical analysis and quantitative statistical metrics. First, m*Chl-a* distribution was visualized via a histogram plotted alongside a map displaying m*Chl-a* values. The normality of the distribution was tested using the Shapiro–Wilk test [27], and descriptive statistics including the global mean ($\overline{X}$), median (m), and standard deviation (*std*) were calculated.

Furthermore, m*Chl-a* was categorized into three classes: values lower than 0.5 mg·m^{-3}, between 1 and 0.5 mg·m^{-3}, and higher than 1 mg·m^{-3}, considering as first boundary the value of *Chl-a* used in the beta version (0.5 mg·m^{-3}); and as second boundary the third quantile of the dataset. A pie chart was utilized to represent the percentage of m*Chl-a* falling into each category.

Additionally, the regional coefficient of variation of *Chl-a* (*Chl-a CV*, Equation (23)) was computed at each region to assess both homogeneity and temporal variability.

$$Chl\text{-}a\ CV = \frac{\sigma}{\mu} \tag{23}$$

where σ represents the standard deviation of the dataset and μ denotes the mean.

Similarly, the regional *CV* of *Chl-a* was mapped, and a histogram was generated to depict its distribution. Additionally, *Chl-a CV* values were grouped into oceanic basins to investigate global variability patterns.

2.6. Sensitivity Analysis

To evaluate the influence of *Chl-a*, depth, and $R_{rs}(560)$ variability on r_b estimation, we generated five synthetic datasets using a revised Saltelli sampling sequence approach [28–31] (Table 2). This method produces quasi-random sequences of size $n \times (2p + 2)$, where p represents the number of input parameters, and n is the baseline sample size. For this study, we selected a sample size of 100, which is considered adequate for reliable index estimation. The synthetic datasets were generated based on the distribution limits of satellite-derived *Chl-a* and $R_{rs}(560)$ observed in the evaluated regions between 1 January 2019 and 31 December 2022. The depth range was delimited from 0 to 10 m to align with the coverage of the Allen Coral Atlas coral reef monitoring system.

Table 2. Description of the datasets produced for the sensitivity analysis and for the evaluation of the comparison satellite-derived *Chl-a* concentration implementing a regional m*Chl-a* vs. using *Chl-a* fixed at 0.5 mg·m^{-3}.

Dataset	*Chl-a* [mg·m^{-3}]	R_{rs}(560) [sr^{-1}]	Depth [m]
$r_{b\text{-syn}}$ *new*	range = [0–20]	0.0105 (fixed)	range = [0–10]
$r_{b\text{-syn}}$ *new* (0–1)	range = [0–1]	range = [0.009–0.012]	range = [0–10]
$r_{b\text{-syn}}$ *new* (0–10)	range = [0–10]	range = [0.009–0.012]	range = [0–10]
$r_{b\text{-syn}}$ *new* (0–20)	range = [0–20]	range = [0.009–0.012]	range = [0–10]
$r_{b\text{-syn}}$ *beta*	0.5 (fixed)	range = [0.009–0.012]	range = [0–10]

To examine the combined impact of *Chl-a* and depth on r_b calculation variability, we generated a synthetic dataset encompassing the entire range of *Chl-a* (0–20 mg·m^{-3}) and depth (0–10 m), and $R_{rs}(560)$ was fixed at its median (0.0105 sr^{-1}). The synthetic data were used to calculate $r_{b\text{-syn}}$ *new*.

Additionally, to further broaden the assessment of r_b calculation sensitivity to *Chl-a* variability, while also considering variable $R_{rs}(560)$ and depth, we generated three additional sets of $r_{b\text{-syn}}$ calculated from synthetic datasets with varying *Chl-a* concentrations: 0 to 1 mg·m^{-3} ($r_{b\text{-syn}}$ *new* (0–1)), 0 to 10 mg·m^{-3} ($r_{b\text{-syn}}$ *new* (0–10)), and 0 to 20 mg·m^{-3} ($r_{b\text{-syn}}$ *new* (0–20)). In each case, we maintained the same sets of $R_{rs}(560)$ and depth, ranging from 0.009 to 0.012 sr^{-1} and m 0 to 10 m, respectively. These datasets of $R_{rs}(560)$ and depth were also utilized to calculate $r_{b\text{-syn}}$ *beta* (with fixed *Chl-a* of 0.5 mg·m^{-3}), and compare it to $r_{b\text{-syn}}$ *new* (0–1), $r_{b\text{-syn}}$ *new* (0–10), and $r_{b\text{-syn}}$ *new* (0–20).

2.7. Comparison of $r_{b\text{-sat}}$ new vs. $r_{b\text{-sat}}$ beta

To better understand the impact of utilizing m*Chl-a* for r_b estimation based on Sentinel-2 L2A/B satellite data, we calculated the mean depth and median $R_{rs}(560)$ for each monitored region between 1 January 2019 and 31 December 2022. Along with the m*Chl-a* calculated to generate the global map and distribution, we estimated the satellite-derived regional mean r_b ($r_{b\text{-sat}}$ *new*). $r_{b\text{-sat}}$ *new* was compared to $r_{b\text{-sat}}$ *beta*, representing r_b calculated using the same depth and R_{rs} (560) values, but with *Chl-a* fixed at 0.5 mg·m^{-3}.

We assessed the disparity between r_b *new* and r_b *beta* calculating the mean absolute percentage difference (*MAPD*) (Equation (24)).

$$MAPD = mean\sum_{i=1}^{N} \frac{|yi - xi|}{xi} \times 100 \quad (24)$$

Here, *yi* corresponds to $r_{b\text{-sat}}$ *new* and *xi* to $r_{b\text{-sat}}$ *beta*. *MAPD* provides insights into the extent of the differences between the two sets of estimations.

3. Results

The validation of m*Chl-a* shows that the satellite-derived *Chl-a* estimation (Figure 2) is reasonable. Nine regions, covering a wide longitudinal range, were effectively matched with in situ *Chl-a* data collected from 2000 to 2022 (Figure 2). These in situ observations were then regionally averaged to obtain m$Chl\text{-}a_{is}$ values (Table 3). Throughout a visual inspection and statistical analysis, the results revealed a strong correlation between the satellite-derived m*Chl-a* values and their corresponding m$Chl\text{-}a_{is}$ (r = 0.86, p-value < 0.05, Figure 2B). This correlation was further supported by an MB of 0.01 and a RMSD of 0.277 mg·m^{-3} (Figure 2). Overall, this validation exercise imparts confidence in the reliability of the model implemented for *Chl-a* concentration estimation within the domains monitored by the Allen Coral Atlas coral bleaching monitoring system.

Table 3. List of *Chl-a* concentration in situ measurements (m$Chl\text{-}a_{is}$) matched with satellite-derived *Chl-a* (m*Chl-a*), showing the number of in situ measurements (N) for each region, the year of in situ sampling, and the standard deviation (*std*) for both satellite (m*Chl-a std*) and in situ (m$Chl\text{-}a_{is}$ *std*) mean regional *Chl-a* concentration.

Region	N	Year	Mean Depth [m]	m$Chl\text{-}a_{is}$ [mg·m^{-3}]	m$Chl\text{-}a_{is}$ *std* [mg·m^{-3}]	m*Chl-a* [mg·m^{-3}]	m*Chl-a std* [mg·m^{-3}]
Aden	7	2001	0	0.382	0.017	0.234	0.081
East Gulf of Thailand	15	2003	0	1.369	1.973	1.945	2.761
Eritrea	4	2001	0	0.678	0.087	0.453	0.152
Florida Keys	293	2011, 2016–2021	1.49	0.087	0.169	0.345	0.758
Gulf of Suez	85	2001	0	0.367	0.327	0.395	0.134
Gulf of Tadjoura	10	2001	0	0.762	0.044	0.372	0.107
Hawaii	1	2017	0	0.002	-	0.086	0.039
Southeast Florida	10	2007, 2012, 2017	4.24	0.004	0.002	0.123	0.045
Western Yemen	77	2001	0	0.657	0.123	0.446	0.176

The m*Chl-a* map, histogram, and bar chart depicting the regions monitored by the Allen Coral Atlas coral reef monitoring system reveal strong spatial variability (Figure 3). Broadly, the Pacific Ocean exhibits the lowest m*Chl-a* concentration, while the Indian Ocean, specifically the Persian Gulf, Indonesia, and Australia, showcases the highest m*Chl-a* values. In contrast, the Caribbean area displays intermediate values. Hence, these findings illustrate the presence of a global gradient of *Chl-a* concentration condition.

The histogram illustrating m*Chl-a* concentration (Figure 3B) highlights a broad range of values from 0.01 to 20 mg·m^{-3}. Notably, the m*Chl-a* distribution diverges from a normal distribution, as confirmed by the Shapiro–Wilk Normality Test (Figure 3B). Moreover, the statistical analysis underscores significant disparities with the 0.5 mg·m^{-3} *Chl-a* value used in the beta version of the atlas. The global mean *Chl-a* concentration (0.81 mg·m^{-3}) surpasses the value of the beta version of the atlas by 62%, while the median concentration (0.26 mg·m^{-3}) is 48% lower compared to the fixed value. Lastly, the standard deviation (1.21 mg·m^{-3}) accentuated the substantial variability in the m*Chl-a* concentrations observed across diverse sites (Figure 3A,C).

In 78.8% of regions, the m*Chl-a* concentration remains below 0.5 mg·m^{-3}, with only 8.4% of regions exhibiting *Chl-a* values ranging between 0.5 and 1 mg·m^{-3}. The remaining subset of regions (12.8%) records notably higher m*Chl-a* concentration, exceeding 1 mg·m^{-3} (Figure 4). Among these regions with *Chl-a* concentration surpassing 1 mg·m^{-3}, a substantial 72% maintain *Chl-a* values below 5 mg·m^{-3}, while 20% feature *Chl-a* levels ranging from 5 to 10 mg·m^{-3} (Figure 4). Only 8% of the regions illustrate *Chl-a* concentration surpassing the 10 mg·m^{-3} threshold (Figure 4).

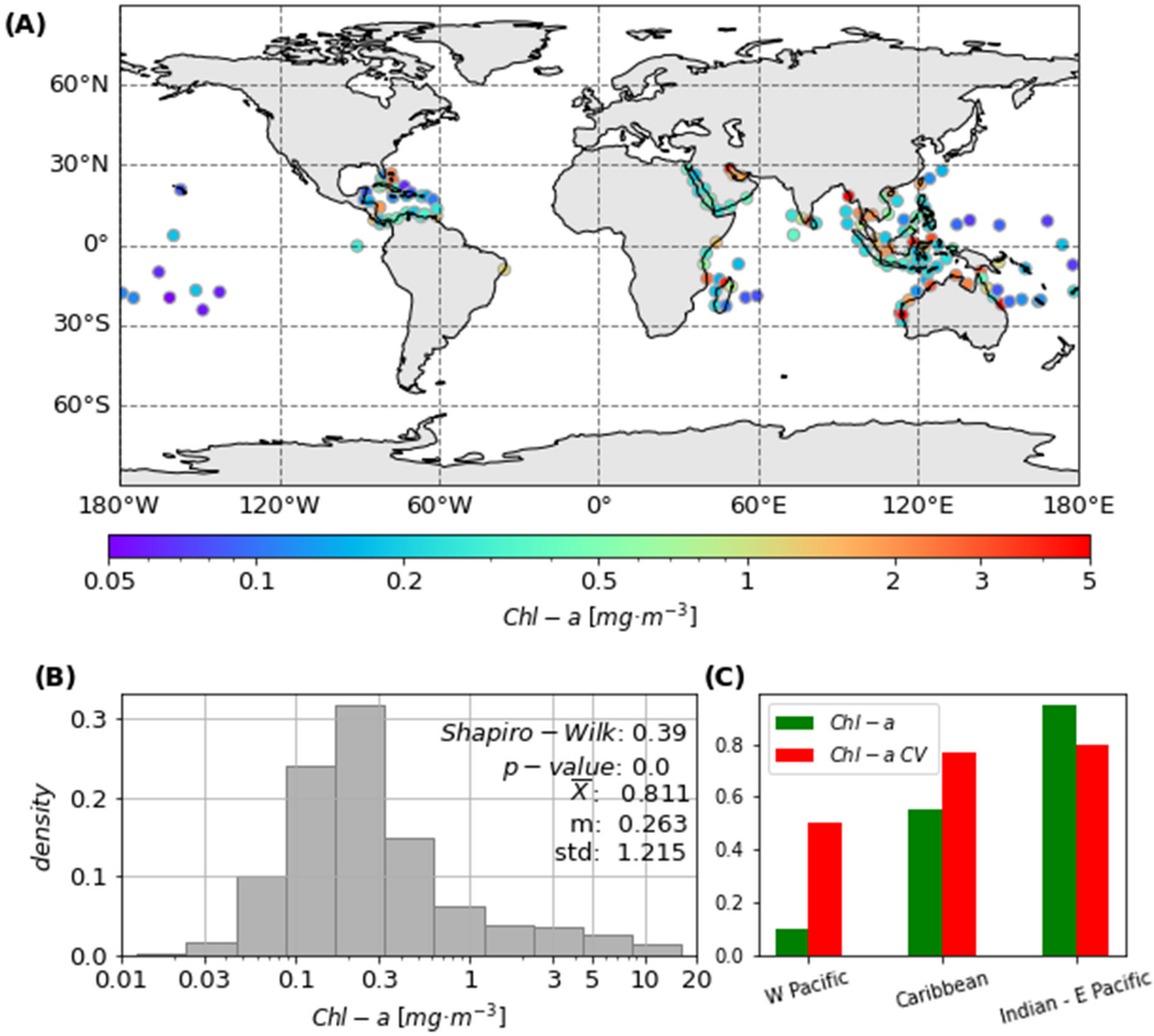

Figure 3. (**A**) Average chlorophyll-a spatial distribution generated for the NOAA CRW regions between January 2019 and December 2022. (**B**) Regional mean *Chl-a* (m*Chl-a*) histogram in logarithmic scale generated for the global coral reefs mapped at the Allen Coral Atlas. $\overline{X}$ represents the mean of global *Chl-a*, *m* is the median and *std* is the standard deviation. (**C**) Bar chart of mean *Chl-a*, and coefficient of variation from the West Pacific Ocean, Caribbean area, Indian Ocean, and East Pacific Ocean.

A global map illustrating the regional coefficient of variation of m*Chl-a* (*Chl-a CV*; Figure 5A,B) indicates, in general, low temporal variability in *Chl-a*. This observation is supported by the histogram (Figure 5B), showing that the majority of *Chl-a CV* values fall below 0.7, with a strong peak at 0.4. However, it is worth noting the presence of a bi-modal distribution, featuring a distinct second peak of *Chl-a CV* values rounding 1.

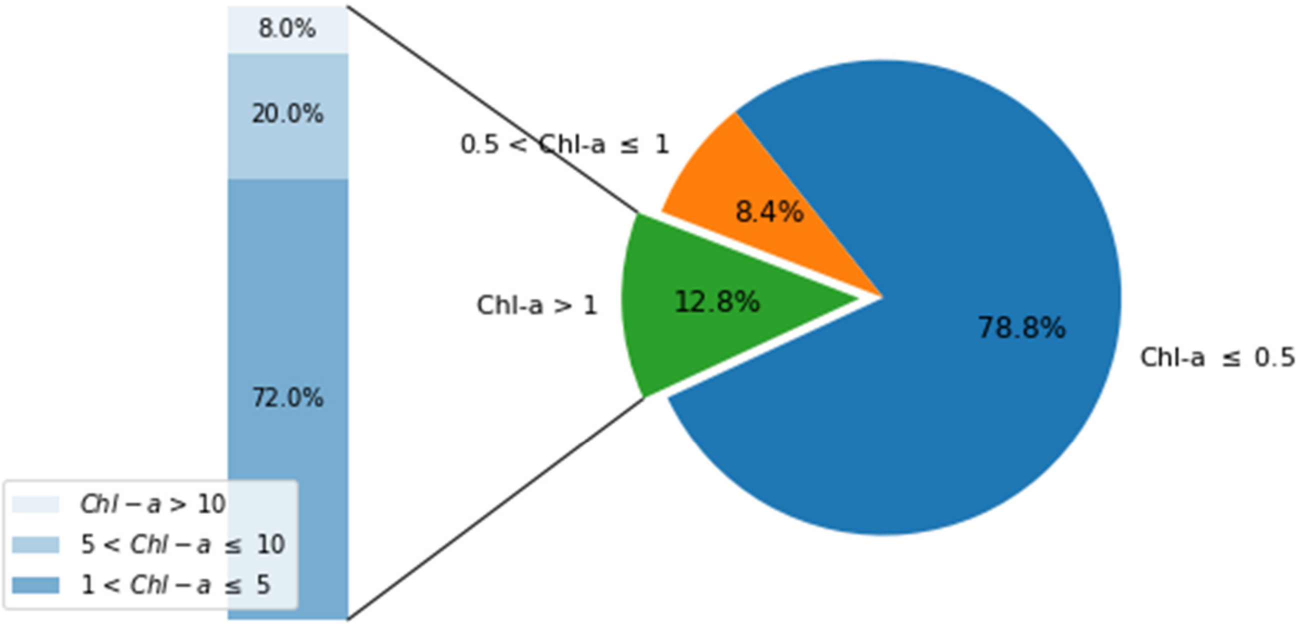

Figure 4. Regional mean Chlorophyll-a [mg·m^{-3}] concentrations segmented into three categories, *Chl-a* $\leq$ 0.5 (blue), 0.5 < *Chl-a* $\leq$ 1 (orange), *Chl-a* > 1 (green). The last category is presented in a bar chart (left) showing 1< *Chl-a* $\leq$ 5 (lower segment), 5 < *Chl-a* $\leq$ 10 (middle segment), and *Chl-a* > 10 (upper segment).

In a more comprehensive analysis, regions exhibiting elevated *Chl-a CV* (>1) were predominantly located within the Indian Ocean, Indonesia, and the Caribbean area. Conversely, regions characterized by low *Chl-a CV* (<1) were distributed across the globe, with prevalence in the Pacific Ocean where m*Chl-a* concentrations remained the lowest (<0.2 mg·m^{-3}; Figure 3A,C). It is noteworthy that, as a general trend, regions displaying low m*Chl-a* level consistently demonstrated greater *Chl-a CV*, as confirmed by the declining m*Chl-a* to *Chl-a CV* (Figure 3C).

Based on the results of the sensitivity analysis, when r_b was calculated using a fixed value of $R_{rs}(560)$, variable depth, and *Chl-a*, the impact of *Chl-a* variability on r_b calculation was more pronounced as the water column deepened. Specifically, this effect became significant when the water column depth exceeded 3 m, and its magnitude increased with higher *Chl-a* values (Figure 6A). This observation was particularly relevant considering that the average depth of the monitored coral reefs was 4.9 $\pm$ 1.87 m, with a substantial 83% of the regions having a depth greater than 3 m.

In the Allen Coral Atlas coral reef monitoring system, r_b calculations for the monitored regions initially employed a fixed *Chl-a* value of 0.5 mg·m^{-3} alongside variable $R_{rs}(560)$ and depth, as mentioned earlier. However, when we compared $r_{b\text{-syn}}$ *beta*, calculated with fixed *Chl-a* of 0.5 mg·m^{-3} and synthetic datasets of $R_{rs}(560)$ and depth, to $r_{b\text{-syn}}$ *new* (0–1), $r_{b\text{-syn}}$ *new* (0–10), and $r_{b\text{-syn}}$ *new* (0–20), which utilized variable *Chl-a* across three different ranges and the same synthetic dataset of $R_{rs}(560)$ and depth, a notable trend emerged. This trend became evident as we observed that the wider the *Chl-a* range employed, the greater the disparity in r_b estimation (Figure 6B). This disparity was evidenced and quantified by the *MAPD*, which recorded values of 8.29%, 13.89%, and 36.46% for $r_{b\text{-syn}}$ *new* (0–1), $r_{b\text{-syn}}$ *new* (0–10), and $r_{b\text{-syn}}$ *new* (0–20) in comparison to $r_{b\text{-syn}}$ *beta*, respectively.

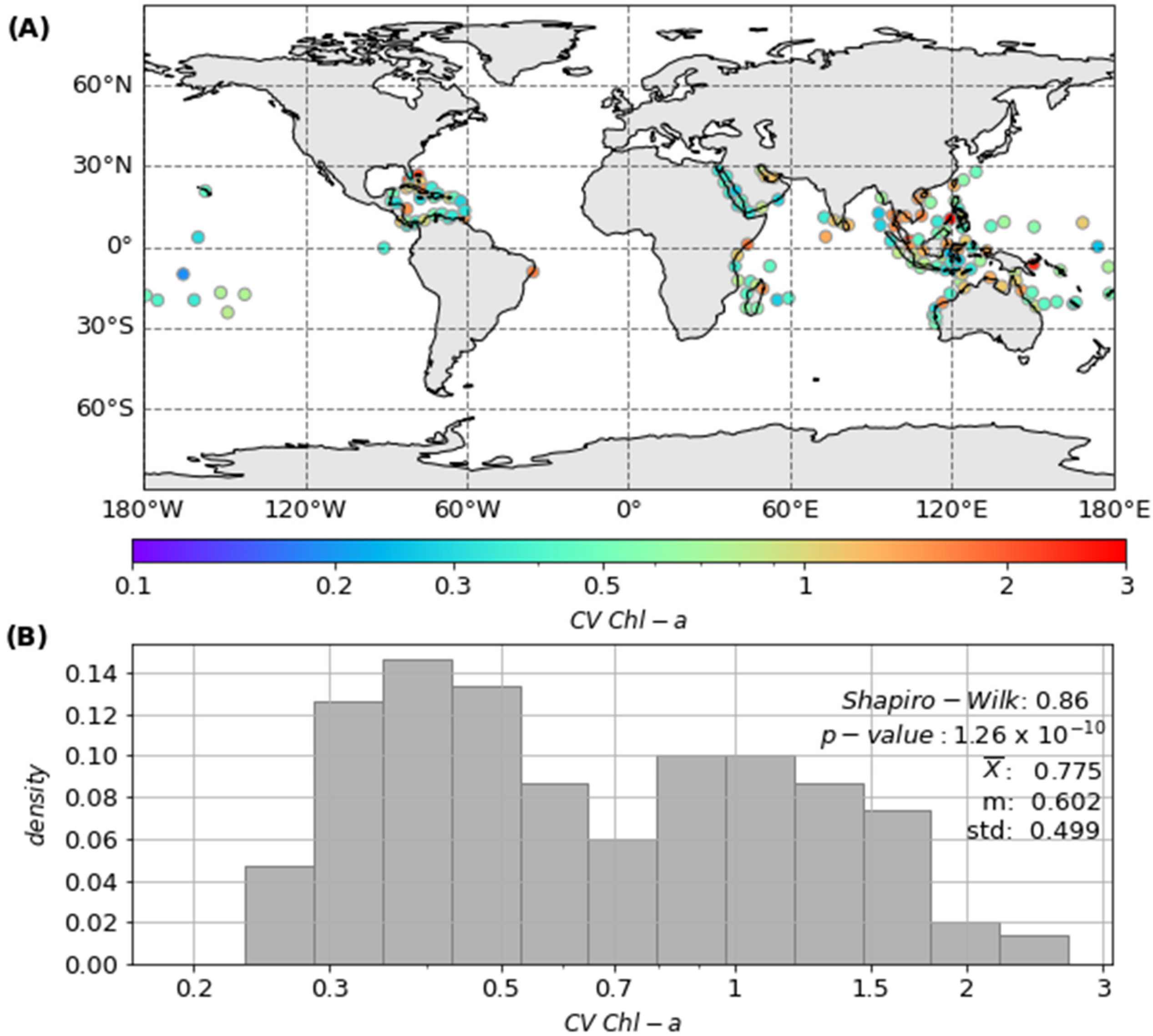

Figure 5. (**A**) Global map of regional *Chl-a* coefficient of variation (CV) in logarithmic scale, (**B**) CV histogram of *Chl-a* in logarithmic scale generated for the global coral reefs mapped at the Allen Coral Atlas.

While the $r_{\text{b-syn}}$ *beta* values remained low, ranging from 0.06 to 0.13, a distinct shift occurred as we extended the range of *Chl-a* values. Notably, $r_{\text{b-syn}}$ *new* (0–1) values also exhibited a limited range, spanning from 0.06 to 0.11, which aligns with $r_{\text{b-syn}}$ beta. However, expanding the *Chl-a* range to 0–10 mg·m^{-3} and 0–20 mg·m^{-3}, substantial variations were observed in the resulting range of the corresponding $r_{\text{b-syn}}$ *new*. An expansion in the range of $r_{\text{b-syn}}$ *new* (0–10) was observed, spanning from 0.06 to 0.22. This variation intensified further in the $r_{\text{b-syn}}$ *new* (0–20) values, which ranged from 0.06 to 0.45.

Furthermore, the comparison between $r_{\text{b-sat}}$ *new*, calculated using m*Chl-a* in conjunction with satellite-derived median $R_{\text{rs}}(560)$ and depth for each pixel, and $r_{\text{b-sat}}$ *beta*, computed with a constant *Chl-a* value of 0.5 mg·m^{-3} alongside the same satellite-derived median $R_{\text{rs}}(560)$ and depth for each pixel (Figure 7) underscored a significant disparity between these two methodologies. When a fixed *Chl-a* value was employed, the resulting r_{b} values were confined within the range of 0.08 to 0.19. However, with variable *Chl-a* considered, the range significantly expanded, encompassing values ranging from 0.09 to 0.58. This divergence amounted to an 18.4% difference in estimation between the two approaches.

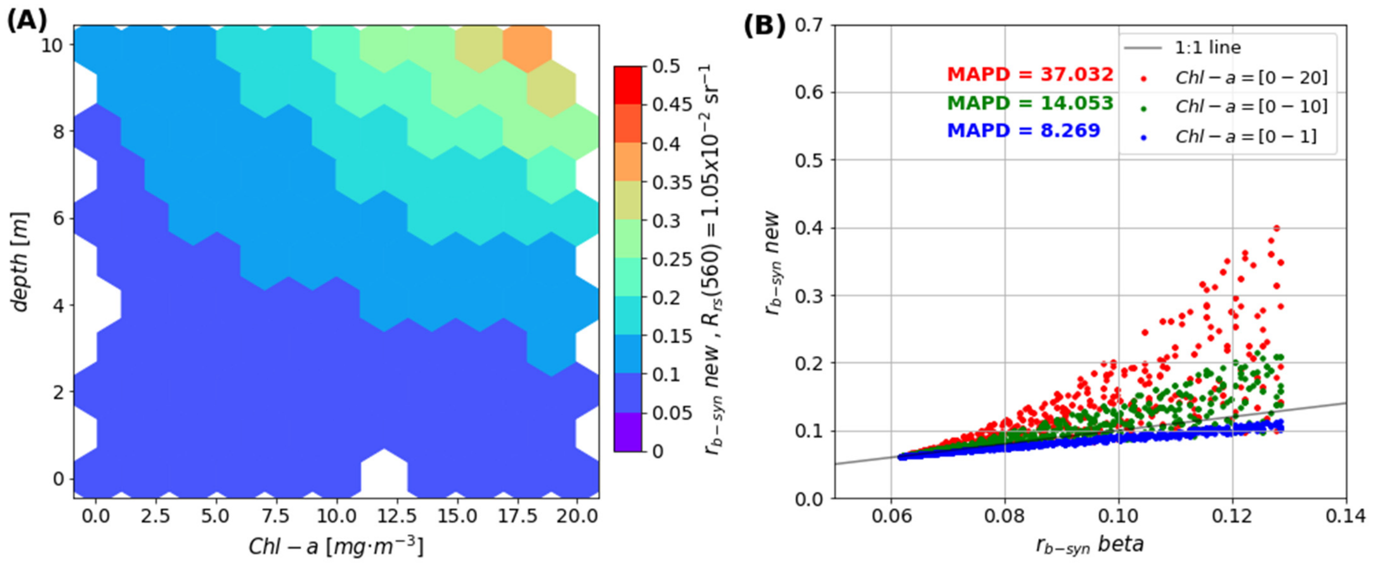

Figure 6. (**A**) Synthetic r_b(560) nm calculated from R_{rs}(560) = 0.0105 sr^{-1}, variable depth (0 to 10 m) and *Chl-a* (0 to 20 mg·m^{-3}). (**B**) Scatterplot showing r_b estimation with variable R_{rs} (560) (0.009 to 0.012 sr^{-1}) and depth (0 to 10 m) implementing r_b *beta* (*Chl-a* = 0.5 mg·m^{-3}) and r_b *new* with three ranges of variable *Chl-a* ([0–1], [0–10], [0–20]).

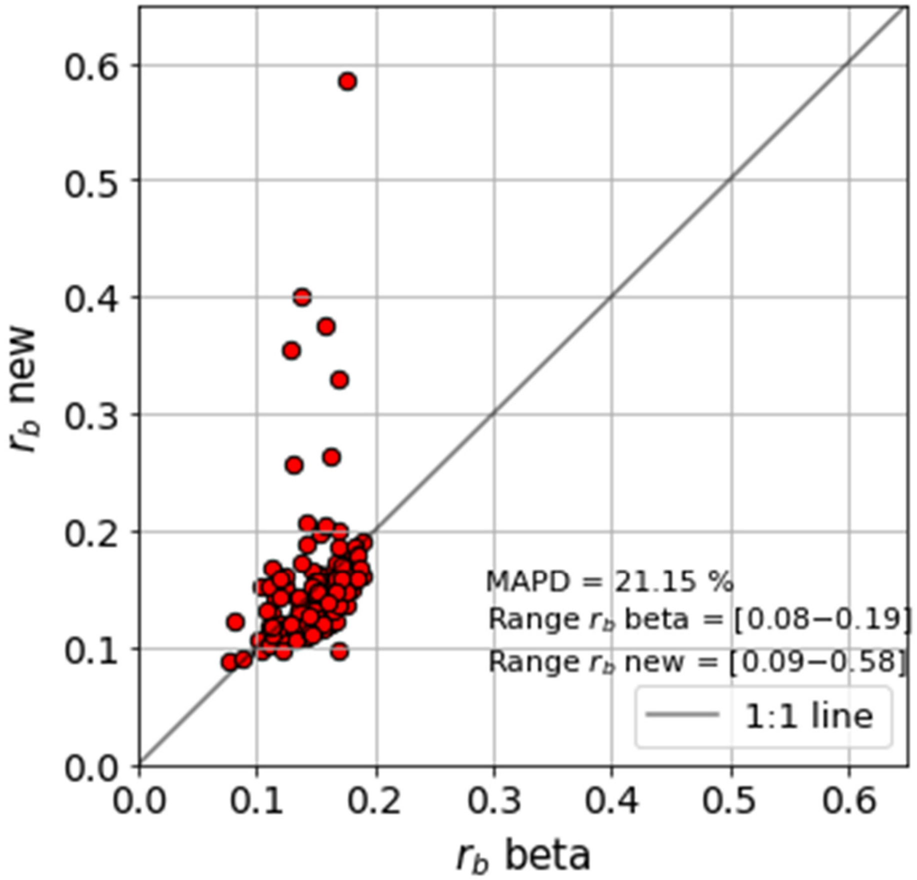

Figure 7. Regional satellite-derived r_b calculated from the regional median of R_{rs}(560) from January 2019 to December 2022, mean regional depth, and the mean regional *Chl-a* (r_b *new*) vs. the calculation with fixed *Chl-a* (0.5 mg·m^{-3}) (r_b *beta*).

4. Discussion

The main purpose of our study was to explore the impact of satellite-derived *Chl-a* concentration variability on the estimation of bottom reflectance (r_b). Our findings underscore the critical importance of using accurate *Chl-a* values in r_b calculations from satellite data, given the significance of *Chl-a* as major input in the computation of $r_{rs}{}^c$ (Figure 1), for which accurate determination is essential for estimates of bottom reflectance [32,33]. In this context, our sensitivity analysis, particularly in regions with depths greater than 3 m, revealed a significant effect of *Chl-a* variability on r_b calculation (Figure 6). Considering that 83% of the monitored coral reefs are situated at depths beyond this threshold (see Section 3), the substantial variability in *Chl-a* among the surveyed coral reefs (Figure 3) emphasizes the need of using accurate *Chl-a* values. Additionally, the comparison of $r_{\text{b-sat}}$ *new* to $r_{\text{b-sat}}$ *beta* confirmed the strong impact of *Chl-a* concentration over satellite-based r_b calculation.

The decision to utilize a model originally designed for Case 1 waters [13] was based on the prevailing oligotrophic oceanic conditions characterizing tropical coral reef ecosystems [34]. Within these tropical domains, continental shelves and island perimeters typically exhibit traits of clear-water environments with low nutrient levels, resulting in constrained phytoplankton biomass [34–37]. This context served as a backdrop for the subsequent validation, which demonstrated reasonable accuracy of the [13] model to predict mean water column *Chl-a* concentration across coral reefs monitored by the Allen Coral Atlas. Furthermore, this finding aligns with previous studies, producing m*Chl-a* estimates that are in line with in situ measurements documented in the existing literature. For instance, a study conducted in Bonaire [38] spanning 2011, 2012, and 2013 reported mean *Chl-a* concentration of 0.128 ± 0.035 mg·m^{-3}, aligning with our estimation for the Aruba, Bonaire, and Curaçao Islands (0.19 ± 0.077 mg·m^{-3}). Similarly, our computed m*Chl-a* in Puerto Rico (0.236 ± 0.228 mg·m^{-3}) corresponds well with findings by [39] reporting concentrations of 0.295 ± 0.287 mg·m^{-3}. In the Red Sea, *Chl-a* concentration presented by [40] for research cruises in 2008, 2010 and 2011 [41–44] (ranging between 0.05 and 0.12 mg·m^{-3}) closely mirror our computation of 0.17 ± 0.06 mg·m^{-3}. Furthermore, our m*Chl-a* estimation for the Persian Gulf (2.329 ± 1.456 mg·m^{-3}) aligns with in situ measurements by [45] (2.17 ± 1.71 mg·m^{-3}) and [46] (2.54 ± 2.16 mg·m^{-3}). In New Caledonia, our calculated m*Chl-a* (0.123 ± 0.409 mg·m^{-3}) closely matches the in situ measurements reported by [47,48] (0.25 ± 0.01 mg·m^{-3}).

Conversely, along the Brazilian coast, m*Chl-a* tends to be overestimated. This region is strongly influenced by precipitations and continental runoff, which have a significant impact on regional biogeochemical processes [49], thereby increasing the optical complexity which affects the estimation of satellite-derived *Chl-a* concentration. This is reflected in the estimation of m*Chl-a*, for instance, in Costa dos Corais, where [50] conducted monthly sampling of in situ data over a year between 2018 and 2019, reporting a mean *Chl-a* concentration of 0.78 ± 0.43 mg·m^{-3}, slightly lower than the satellite-derived m*Chl-a* (1.191 ± 1.973 mg·m^{-3}). Furthermore, m*Chl-a in* the Abrolhos reef was highly overestimated compared to observations by [51] (0.92 ± 1.1 mg·m^{-3} vs. 0.22 ± 0.08 mg·m^{-3}). However, it is important to note that the results reported by [51] were based on in situ data collected solely in July 2019, supplemented with 8-day *Chl-a* data from the MODIS Aqua sensor spanning from 2003 to 2019. Given the temporal limitations of the in situ data, they may not fully capture the overall characteristics of the region. Additionally, because of the low spatial resolution (4 km) of the sensor's L3 product, the features and variability of this small region are averaged and smoothed, potentially resulting in under/over-estimations of *Chl-a* concentration [52].

In line with previous studies [53,54], our findings reveal significant spatial variability in m*Chl-a* concentrations across the globally distributed coral reefs monitored by the Allen Coral Atlas, ranging from 0.01 to 20 mg·m^{-3} (Figures 3 and 4). Upon examination of specific oceanic basins, our results align with evidence indicating lower productivity in the central Pacific Ocean compared to other oceanic regions [55–57]. Furthermore, our findings in the Equatorial Pacific region are in agreement with previous observations, showing *Chl-a* concentrations ranging from 0.08 to 0.6 mg·m^{-3} with low temporal variability [58–60]. In contrast, the Indian Ocean and West Pacific exhibit the highest *Chl-a* concentrations and variability (*Chl-a CV*). Reports from the West Pacific region further support our results, indicating high *Chl-a* concentrations and significant variability [61–64]. The strong variability observed in the Indian Ocean and West Pacific is also consistent with global studies conducted by [56] and later by [65]. Finally, our results in the Caribbean region are consistent with a previous study in the U.S. Virgin Islands, which reported *Chl-a* values ranging from 0.06 to 0.79 mg·m^{-3} (±0.16 mg·m^{-3}) [66].

In summary, our analysis indicates that the impact of *Chl-a* variability on r_b calculation becomes significant only when the water column depth exceeds 3 m, suggesting that, for shallower regions, the utilization of a regional *Chl-a* value rather than a global one is optional. Nevertheless, it is important to acknowledge certain limitations of the implemented model, particularly in optically complex waters strongly influenced by terrestrial factors. For instance, along the Brazilian coast, where land runoff has a significant impact on the water's optical characteristics. In these regions, the model may overestimate *Chl-a* concentration, thereby impacting the estimation of r_b. This underscores the need for caution and further refinement of the model when applied in environments with high optical complexity and strong land influence. Therefore, further analysis should be undertaken to assess the interference and impact of other optically active components in the water, such as colored dissolved organic carbon, and suspended particulate matter, on the estimation of r_b.

5. Conclusions

We developed a novel approach to estimate r_b for the Allen Coral Atlas coral reef monitoring system by leveraging m*Chl-a* values instead of a fixed global mean value of 0.5 mg·m^{-3}. Initially, we estimated the regional *Chl-a* values, analyzed their distribution, and evaluated their impact on r_b calculation. Subsequently, we compared the resultant r_b values with those derived from a constant *Chl-a* of 0.5 mg·m^{-3}.

Our research yielded several significant discoveries. Firstly, we found that *Chl-a* does not conform to a Gaussian distribution in global coral reef areas, indicating that a global mean value does not adequately represent local *Chl-a* concentration across all regions. Secondly, we observed that r_b estimation becomes particularly sensitive to *Chl-a* concentration when the water column depth exceeds 3 m, a scenario present in over 83% of monitored reefs. Lastly, our analysis revealed that the implementation of m*Chl-a* value in r_b calculation leads to an 18.4% difference compared to results obtained using the global mean *Chl-a* 0.5 mg·m^{-3}.

These findings underscore the significance of incorporating regional mean *Chl-a* values to enhance the accuracy of r_b calculation, thereby strengthening the foundation of the bleaching monitoring system of the Allen Coral Atlas.

Author Contributions: Conceptualization, A.G.B. and G.P.A.; methodology, A.G.B.; software, A.G.B.; validation, A.G.B.; formal analysis, A.G.B.; resources, P.N.; data curation, P.N.; writing—original draft preparation, A.G.B.; writing—review and editing G.P.A.; supervision, G.P.A.; project administration, P.M. and G.P.A.; funding acquisition, G.P.A. All authors have read and agreed to the published version of the manuscript.

Funding: This research was funded by Vulcan Inc., grant number 46459.

Institutional Review Board Statement: Not applicable.

Informed Consent Statement: Not applicable.

Data Availability Statement: All data supporting the findings of this study are openly available. References to the datasets analyzed or generated during our research are cited within the body of this manuscript. These datasets are hosted on publicly accessible repositories, where they can be accessed freely by the academic community and the general public. For detailed information on the data sources and their respective access links, please refer to the References section of this article.

Acknowledgments: We would like to acknowledge and express our appreciation to Marcel König who contributed to the review of the initial draft.

Conflicts of Interest: The authors declare no conflicts of interest. The funders had no role in the design of the study; in the collection, analyses, or interpretation of data; in the writing of the manuscript; or in the decision to publish the results.

References

1. Mulhall, M. Saving the rainforests of the sea: An analysis of international efforts to conserve coral reefs. *Duke Environ. Law Policy Forum.* **2009**, *19*, 321–351.
2. Where are Corals Found? NOAA Coral Reef Conservation Program. National Oceanic and Atmospheric Administration (NOAA). Available online: http://coralreef.noaa.gov/aboutcorals/coral101/corallocations/ (accessed on 19 December 2023).
3. Spalding, M.D.; Grenfell, A.M. New estimates of global and regional coral reef areas. *Coral Reefs* **1997**, *16*, 225–230. [CrossRef]
4. Spalding, M.D.; Ravilious, C.; Green, P.E. *World Atlas of Coral Reefs*; University of California Press: Berkley, CA, USA, 2001; Volume 39. [CrossRef]
5. Pendleton, L.; Wilson, M.A.; Farber, S.; Colgan, C.S.; Lipton, D.; Kasperski, S.; Dismukes, D.E.; Barnett, M.L.; Darb, K.A.R.; Jin, D.; et al. The Economic and Market Value of Coasts and Estuaries: What's at Stake? (Pendleton LH, ed.). Restore America's Estuaries; 2010; Volume 182. Available online: https://repository.library.noaa.gov/view/noaa/10108/noaa_10108_DS1.pdf (accessed on 28 September 2023).
6. Schill, S.; Knowles, J.; Rowlands, G.; Margles, S.; Agostini, V.; Blyther, R. Coastal Benthic Habitat Mapping to Support Marine Resource Planning and Management in St. *Kitts and Nevis. Geogr. Compass* **2011**, *5*, 898–917. [CrossRef]
7. Stolt, M.; Bradley, M.; Turenne, J.; Payne, M.; Scherer, E.; Cicchetti, G.; Shumchenia, E.; Guarinello, M.; King, J.; Boothroyd, J.; et al. Mapping Shallow Coastal Ecosystems: A Case Study of a Rhode Island Lagoon. *J. Coast. Res.* **2011**, *27*, 1–15. [CrossRef]
8. Barbier, E.B.; Koch, E.W.; Silliman, B.R.; Hacker, S.D.; Wolanski, E.; Primavera, J.; Granek, E.F.; Polasky, S.; Aswani, S.; Cramer, L.A.; et al. Coastal ecosystem-based management with nonlinear ecological functions and values. *Science* **2008**, *319*, 321–323. [CrossRef] [PubMed]
9. Zhang, C. Applying data fusion techniques for benthic habitat mapping and monitoring in a coral reef ecosystem. *ISPRS J. Photogramm. Remote Sens.* **2015**, *104*, 213–223. [CrossRef]
10. Ma, Y.; Zhang, H.; Li, X.; Wang, J.; Cao, W.; Li, D.; Lou, X.; Fan, K. An exponential algorithm for bottom reflectance retrieval in clear optically shallow waters from multispectral imagery without ground data. *Remote Sens.* **2021**, *13*, 1169. [CrossRef]
11. Xu, Y.; Vaughn, N.R.; Knapp, D.E.; Martin, R.E.; Balzotti, C.; Li, J.; Foo, S.A.; Asner, G.P. Coral bleaching detection in the hawaiian islands using spatio-temporal standardized bottom reflectance and planet dove satellites. *Remote Sens.* **2020**, *12*, 3219. [CrossRef]
12. Dubinsky, Z.; Stambler, N. *Coral Reefs: An Ecosystem in Transition*; Springer Science and Business Media LLC: Dordrecht, The Netherlands, 2011. [CrossRef]
13. Hu, C.; Lee, Z.; Franz, B. Chlorophyll a algorithms for oligotrophic oceans: A novel approach based on three-band reflectance difference. *J. Geophys. Res. Ocean.* **2012**, *117*, C01011. [CrossRef]
14. Angal, A.; Xiong, X.; Shrestha, A. Cross-calibration of MODIS reflective solar bands with sentinel 2A/2B MSI instruments. *IEEE Trans. Geosci. Remote Sens.* **2020**, *58*, 5000–5007. [CrossRef]
15. O'Reilly, J.E.; Werdell, P.J. Chlorophyll algorithms for ocean color sensors—OC4, OC5 & OC6. *Remote Sens. Environ.* **2019**, *229*, 32–47. [CrossRef] [PubMed]
16. Li, J.; Fabina, N.S.; Knapp, D.E.; Asner, G.P. The sensitivity of multi-spectral satellite sensors to benthic habitat change. *Remote Sens.* **2020**, *12*, 532. [CrossRef]
17. Lee, Z.; Carder, K.L.; Mobley, C.D.; Steward, R.G.; Patch, J.S. Hyperspectral Remote Sensing for Shallow Waters. I. A Semianalytical. Model. *Appl. Opt.* **1998**, *37*, 6329–6338. [CrossRef] [PubMed]
18. Li, J.; Knapp, D.E.; Lyons, M.; Roelfsema, C.; Phinn, S.; Schill, S.R.; Asner, G.P. Automated global shallowwater bathymetry mapping using google earth engine. *Remote Sens.* **2021**, *13*, 1469. [CrossRef]
19. Lee, Z.; Carder, K.L.; Mobley, C.D.; Steward, R.G.; Patch, J.S. Hyperspectral remote sensing for shallow waters: 2 Deriving bottom depths and water properties by optimization. *Appl. Opt.* **1999**, *38*, 3831. [CrossRef]
20. Pope, R.M.; Fry, E.S. Absorption spectrum (380–700 nm) of pure water. II. Integrating cavity measurements. *Appl. Opt.* **1997**, *36*, 8710–8723. [CrossRef]
21. Lee, Z.; Weidemann, A.; Arnone, R. Combined effect of reduced band number and increased bandwidth on shallow water remote sensing: The case of world view 2. *IEEE Trans Geosci Remote Sens.* **2013**, *51*, 2577–2586. [CrossRef]
22. Lee, Z.; Lubac, B.; Werdell, J.; Arnone, R. An Update of the Quasi-Analytical Algorithm (QAA_v5). 2009, IOCCG software report. Available online: http://www.ioccg.org/groups/Software_OCA/QAA_v5.pdf (accessed on 19 August 2023).
23. Bricaud, A.; Morel, A.; Babin, M.; Allali, K.; Claustre, H. Variations of light absorption by suspended particles with chlorophyll a concentration in oceanic (case 1) waters: Analysis and implications for bio-optical models. *J. Geophys. Res. Ocean.* **1998**, *103*, 31033–31044. [CrossRef]

24. Morel, A.; Maritorena, S. Bio-optical properties of oceanic waters: A reappraisal. *J. Geophys. Res. Ocean.* **2001**, *106*, 7163–7180. [CrossRef]
25. Smith, R.C.; Baker, K.S. Optical properties of the clearest natural waters (200–800 nm). *Appl. Opt.* **1981**, *20*, 177–184. [CrossRef]
26. Werdell, P.J.; Bailey, S.; Fargion, G.; Pietras, C.; Knobelspiesse, K.; Feldman, G.; McClain, C. Unique data repository facilitates ocean color satellite validation. *EOS Trans. AGU* **2003**, *84*, 377–387. [CrossRef]
27. Shapiro, S.S.; Wilk, M.B. An analysis of variance test for normality (complete samples). *Biometrika* **1965**, *52*, 591–611. [CrossRef]
28. Campolongo, F.; Saltelli, A.; Cariboni, J. From screening to quantitative sensitivity analysis. A unified approach. *Comput. Phys. Commun.* **2011**, *182*, 978–988. [CrossRef]
29. Owen, A.B. On Dropping the First Sobol' Point. *Springer Proc. Math. Stat.* **2022**, *387*, 71–86. [CrossRef]
30. Saltelli, A. Making best use of model evaluations to compute sensitivity indices. *Comput. Phys. Commun.* **2002**, *145*, 280–297. [CrossRef]
31. Sobol, I.M. Global sensitivity indices for nonlinear mathematical models and their Monte Carlo estimates. *Math. Comput. Simul.* **2001**, *55*, 271–280. [CrossRef]
32. Li, J.; Yu, Q.; Tian, Y.Q.; Becker, B.L.; Siqueira, P.; Torbick, N. Spatio-temporal variations of CDOM in shallow inland waters from a semi-analytical inversion of Landsat-8. *Remote Sens. Environ.* **2018**, *218*, 189–200. [CrossRef]
33. Reichstetter, M.; Fearns, P.; Weeks, S.; McKinna, L.; Roelfsema, C.; Furnas, M. Bottom Reflectance in Ocean Color Satellite Remote Sensing for Coral Reef Environments. *Remote Sens.* **2015**, *7*, 16756–16777. [CrossRef]
34. Birkeland, C. Caribbean and Pacific Coastal marine system: Similarities and differences. *Nat. Resour.* **1990**, *26*, 3–12.
35. Kidd, R.; Sander, F. Influence of Amazon River discharge on the marine production system off Barbados, West Indies. *J. Mar. Res.* **1981**, *37*, 669–682.
36. Bienfang, P.K.; Szyper, J.P.; Okamoto, M.Y.; Noda, E.K. Temporal and spatial variability of phytoplankton in a subtropical ecosystem. *Limnol. Oceanogr.* **1984**, *29*, 527–539. [CrossRef]
37. Tranter, D.J.; Leech, G.S. Factors influencing the standing crop of phytoplankton on the Australian Northwest Shelf seaward of the 40 m isobath. *Cont. Shelf Res.* **1987**, *7*, 115–133. [CrossRef]
38. Slijkerman, D.M.E.; de León, R.; de Vries, P. A baseline water quality assessment of the coastal reefs of Bonaire, Southern Caribbean. *Mar. Pollut. Bull.* **2014**, *86*, 523–529. [CrossRef] [PubMed]
39. Otero, E.; Carbery, K.K. Revista de Biología Tropical Chlorophyll a and turbidity patterns over coral reefs systems of La Parguera Natural Reserve, Puerto. *J. Trop. Biol.* **2005**, *53*, 25–32. Available online: http://www.redalyc.org/articulo.oa?id=44920889003 (accessed on 15 July 2023).
40. Racault, M.-F.; Raitsos, D.E.; Berumen, M.L.; Brewin, R.J.; Platt, T.; Sathyendranath, S.; Hoteit, I. Phytoplankton phenology indices in coral reef ecosystems: Application to ocean-color observations in the Red Sea. *Remote Sens. Environ.* **2015**, *160*, 222–234. [CrossRef]
41. Brewin, R.J.W.; Raitsos, D.E.; Pradhan, Y.; Hoteit, I. Comparison of chlorophyll in the Red Sea derived from MODIS-Aqua and in vivo fluorescence. *Remote Sens. Environ.* **2013**, *136*, 218–224. [CrossRef]
42. Barbini, R.; Colao, F.; De Dominicis, L.; Fantoni, R.; Fiorani, L.; Palucci, A.; Artamonov, E.S. Analysis of simultaneous chlorophyll measurements by lidar fluorosensor, MODIS and SeaWiFS. *Int. J. Remote Sens.* **2004**, *25*, 2095–2110. [CrossRef]
43. Boss, E.; Picheral, M.; Leeuw, T.; Chase, A.; Karsenti, E.; Gorsky, G.; Taylor, L.; Slade, W.; Ras, J.; Claustre, H. The characteristics of particulate absorption, scattering and attenuation coefficients in the surface ocean; Contribution of the Tara Oceans expedition. *Methods Oceanogr.* **2013**, *7*, 52–62. [CrossRef]
44. Werdell, P.J.; Proctor, C.W.; Boss, E.; Leeuw, T.; Ouhssain, M. Underway sampling of marine inherent optical properties on the Tara Oceans expedition as a novel resource for ocean color satellite data product validation. *Methods Oceanogr.* **2013**, *7*, 40–51. [CrossRef]
45. Ghaemi, M.; Abtahi, B.; Gholamipour, S. Spatial distribution of nutrients and chlorophyll a across the Persian Gulf and the Gulf of Oman. *Ocean Coast. Manag.* **2021**, *201*, 105476. [CrossRef]
46. Polikarpov, I.; Saburova, M.; Al-Yamani, F. Diversity and distribution of winter phytoplankton in the Arabian Gulf and the Sea of Oman. *Cont. Shelf Res.* **2016**, *119*, 85–99. [CrossRef]
47. Dupouy, C.; Wattelez, G.; Fuchs, R.; Murakami, H.; Frouin, R. The colour of the Coral Sea. In Proceedings of the 12th International Coral Reef Symposium, Cairns, Australia, 9–13 July 2012. [CrossRef]
48. Wattelez, G.; Dupouy, C.; Mangeas, M.; Lefèvre, J.; Touraivane Frouin, R. A statistical algorithm for estimating chlorophyll concentration in the New Caledonian lagoon. *Remote Sens.* **2016**, *8*, 45. [CrossRef]
49. Rubio-Cisneros, N.T.; Herrera-Silveira, J.; Morales-Ojeda, S.; Moreno-Báez, M.; Montero, J.; Pech-Cárdenas, M. Water quality of inlets' water bodies in a growing touristic barrier reef Island "Isla Holbox" at the Yucatan Peninsula. *Reg. Stud. Mar. Sci.* **2018**, *22*, 112–124. [CrossRef]
50. Silva, B.J.; Ibánhez, J.S.P.; Pinheiro, B.R.; Ladle, R.J.; Malhado, A.C.; Pinto, T.K.; Flores-Montes, M.J. Seasonal influence of surface and underground continental runoff over a reef system in a tropical marine protected area. *J. Mar. Syst.* **2022**, *226*, 103660. [CrossRef]
51. Barroso, H.d.S.; Lima, I.d.O.; Bezerra, A.D.A.; Garcia, T.M.; Tavares, T.C.L.; Alves, R.S.; Junior, E.F.d.S.; Teixeira, C.E.P.; Viana, M.B.; Soares, M.O. Distribution of nutrients and chlorophyll across an equatorial reef region: Insights on coastal gradients. *Ocean Coast. Res.* **2023**, *71* (Suppl. 2), e23002. [CrossRef]

52. Cazzaniga, I.; Bresciani, M.; Colombo, R.; Della Bella, V.; Padula, R.; Giardino, C. A comparison of Sentinel-3-OLCI and Sentinel-2-MSI-derived Chlorophyll-a maps for two large Italian lakes. *Remote Sens. Lett.* **2019**, *10*, 978–987. [CrossRef]
53. Smith, B.; Pahlevan, N.; Schalles, J.; Ruberg, S.; Errera, R.; Ma, R.; Giardino, C.; Bresciani, M.; Barbosa, C.; Moore, T.; et al. A Chlorophyll-a Algorithm for Landsat-8 Based on Mixture Density Networks. *Front. Remote Sens.* **2021**, *1*, 623678. [CrossRef]
54. Tran, M.D.; Vantrepotte, V.; Loisel, H.; Oliveira, E.N.; Tran, K.T.; Jorge, D.; Mériaux, X.; Paranhos, R. Band Ratios Combination for Estimating Chlorophyll-a from Sentinel-2 and Sentinel-3 in Coastal Waters. *Remote Sens.* **2023**, *15*, 1653. [CrossRef]
55. Gregg, W.W.; Conkright, M.E. Decadal changes in global ocean chlorophyll. *Geophys. Res. Lett.* **2002**, *29*, 20-1–20-4. [CrossRef]
56. Gregg, W.W.; Conkright, M.E. Recent trends in global ocean chlorophyll. *Geophys. Res. Lett.* **2005**, *32*, 1–5. [CrossRef]
57. Vantrepotte, V.; Loisel, H.; Mélin, F.; Desailly, D.; Duforêt-Gaurier, L. Global particulate matter pool temporal variability over the SeaWiFS period (1997–2007). *Geophys. Res. Lett.* **2011**, *38*, 1–5. [CrossRef]
58. Bonelli, A.G.; Vantrepotte, V.; Jorge, D.S.F.; Demaria, J.; Jamet, C.; Dessailly, D.; Mangin, A.; D'Andon, O.F.; Kwiatkowska, E.; Loisel, H. Colored dissolved organic matter absorption at global scale from ocean color radiometry observation: Spatio-temporal variability and contribution to the absorption budget. *Remote Sens. Environ.* **2021**, *265*, 112637. [CrossRef]
59. Jönsson, B.F.; Salisbury, J.; Atwood, E.C.; Sathyendranath, S.; Mahadevan, A. Dominant timescales of variability in global satellite chlorophyll and SST revealed with a MOving Standard deviation Saturation (MOSS) approach. *Remote Sens. Environ.* **2023**, *286*, 113404. [CrossRef]
60. Pittman, N.A.; Strutton, P.G.; Johnson, R.; Matear, R.J. An Assessment and Improvement of Satellite Ocean ColorAlgorithms for the Tropical Pacific Ocean. *J. Geophys. Res. Ocean.* **2019**, *124*, 9020–9039. [CrossRef]
61. Nababan, B.; Rosyadi, N.; Manurung, D.; Natih, N.M.; Hakim, R. The Seasonal Variability of Sea Surface Temperature and Chlorophyll-a Concentration in the South of Makassar Strait. *Procedia Environ. Sci.* **2016**, *33*, 583–599. [CrossRef]
62. Sachoemar, S. Variability Of Sea Surface Chlorophyll-a, Temperature and Fish Catch Within Indonesian Region Revealed By Satellite Data. *Mar. Res. Indones.* **2015**, *37*, 75–87. [CrossRef]
63. Susanto, D.R.; Marra, J. Effect of the 1997/98 El Niño on Chlorophyll-a Variability Along the Southern Coasts of Java and Sumatra. *Oceanography* **2005**, *18*, 124–127. [CrossRef]
64. Yu, Y.; Xing, X.; Liu, H.; Yuan, Y.; Wang, Y.; Chai, F. The variability of chlorophyll-a and its relationship with dynamic factors in the basin of the South China Sea. *J. Mar. Syst.* **2019**, *200*, 103230. [CrossRef]
65. Vantrepotte, V.; Mélin, F. Inter-annual variations in the SeaWiFS global chlorophyll a concentration (1997-2007). *Deep. Res. Part I Oceanogr. Res. Pap.* **2011**, *58*, 429–441. [CrossRef]
66. Ali, K.A.; Flanagan, D.C.; Brandt, M.E.; Ortiz, J.D.; Smith, T.B. Semi-analytical inversion modelling of Chlorophyll a variability in the U.S. Virgin Islands. *Front. Remote Sens.* **2023**, *4*, 1172819. [CrossRef]